Article

Strain-durable dark current in near-infrared organic photodetectors for skin-conformal photoplethysmographic sensors

Skin-Conformal Photoplethysmographic Sensors

Strain-Durable Dark Current !

J (A/cm²)

Forward
Backward

J_D

Tensile strain (%)

NIR light

Skin-Conformal PPG Signal

Signal (μA)

Time (sec)

Hyeong Ju Eun,
Hanbee Lee,
Yeongseok Shim,
..., Junseok Heo,
Sungjun Park,
Jong H. Kim

sj0223park@ajou.ac.kr (S.P.)
jonghkim@ajou.ac.kr (J.H.K.)

Highlights
Significant reduction of dark current was achieved from PTB7-Th:Y6 NIR OPDs

The developed OPD exhibited strain-durable dark current

OPDs efficiently operated on ultra-thin substrates

Skin-conformal PPG sensors were demonstrated based on the developed OPDs
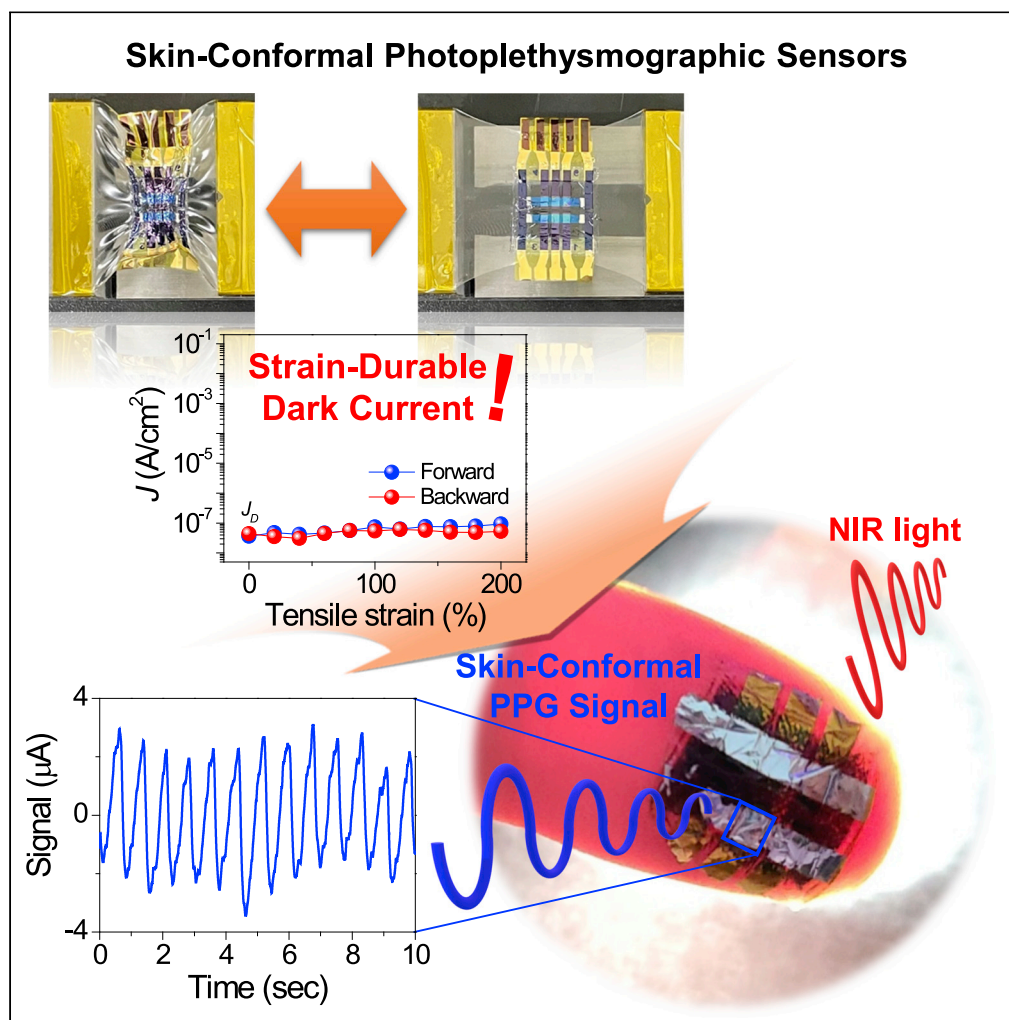
Article

Strain-durable dark current in near-infrared organic photodetectors for skin-conformal photoplethysmographic sensors

Hyeong Ju Eun,[1,3] Hanbee Lee,[2,3] Yeongseok Shim,[2] Gyeong Uk Seo,[1] Ah Young Lee,[1] Jong Jin Park,[1] Junseok Heo,[2] Sungjun Park,[2,*] and Jong H. Kim[1,4,*]

SUMMARY

Sensitive detection of near-infrared (NIR) light is applicable to variety of optical, chemical, and biomedical sensors. Of these diverse applications, NIR photodetectors have been used as a key component for photoplethysmography (PPG) sensors. In particular, because NIR organic photodetectors (OPDs) enable fabrication of stretchable and skin-conformal PPG sensors, they are attaining tremendously increasing interest in both academia and industry. Herein, we report strain-durable and highly sensitive NIR OPDs using an organic bulk heterojunction (BHJ) layer. For effective suppression of dark current, we employed BHJ combination consisting of PTB7-Th:Y6 which forms high energy barrier against transport-injected holes. The optimized OPDs exhibited high specific detectivity up to 2.2×10^{12} Jones at 800 nm. By constructing the devices on the parylene substrates, we successfully demonstrated stretchable NIR OPDs and high-performance skin-conformal PPG sensors.

INTRODUCTION

Development of high-detectivity near-infrared photodetectors (NIR PDs) have received significant attention in recent years because of their diverse applications including NIR image sensors, thermal detectors, biomedical sensors, and telecommunication devices (Liu et al., 2021a, 2021b; Li et al., 2019a; Meng et al., 2021; Chow and Someya, 2020). For demonstrating high-performance NIR PDs, various types of low-bandgap inorganic semiconductors absorbing long wavelengths lights, such as Si, GaAs, InSb, HgCdTe, and CdZnTe, have been developed (Lu et al., 2018; Wang et al., 2021; Li et al., 2016; Shkir et al., 2019; Zhang et al., 2020). Despite their applicability as NIR sensitizers, NIR PDs based on these materials suffer from fabrication complexity, high-cost process, inherent low absorption coefficient, and low mechanical flexibility (Michel et al., 2010; Chen et al., 2016). To overcome these problems, π-conjugated polymers (CPs) and small molecules (SMs) possessing high absorption coefficients in NIR ranges have been intensively investigated. In addition to optical merits, owing to low-cost and high-throughput production using solution processes, and wearable sensor applicability, NIR PDs based on the organic semiconductors are gaining enormous interest (Wei et al., 2021; Huang et al., 2020; Lv et al., 2020; Lee et al., 2019; Park et al., 2018).

However, these NIR OPDs have encountered a severe challenge of high-level and non-controllable dark current density (J_D) under reverse bias (Wu et al., 2020; Liu et al., 2012; Li et al., 2019b). This problem becomes worse on the flexible or stretchable substrates which are essential component for wearable electronics in particular for photoplethysmography (PPG) sensors based on NIR OPDs. To suppress degree of J_D in NIR OPDs, energy level tailoring for NIR-light-absorbing CPs and SMs has been carried out through organic synthesis (Lee et al., 2019; Simone et al., 2020; Kang et al., 2020), while designing device architecture has been also tried such as employing charge blocking layers (Zhou et al., 2015; Yang et al., 2021) or structural engineering in photomultiplication (PM)-type PDs (Zhao et al., 2021a; Liu et al., 2021a, 2021b). However, development of new materials every time is less competitive due to its complicated procedures, and little amount of charge carriers is still injected (Guo et al., 2020) even with charge blocking layers by tunneling process under high reverse bias. Thus, development of a simple approach for mitigating J_D in NIR OPDs is highly desired.

In this article, we suggest a strategic material combination of existing electron-donating CP (PTB7-Th) and electron-accepting SM (Y6) for bulk heterojunction (BHJ) in NIR OPDs, which enables a low level of J_D and

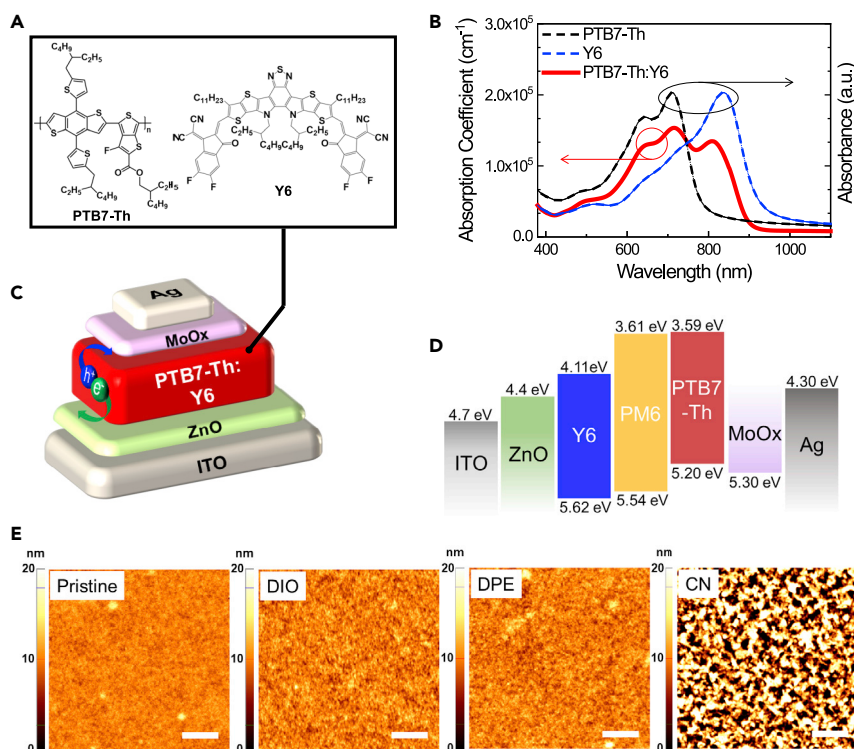[1]Department of Molecular Science and Technology, Ajou University, Suwon 16449, Republic of Korea

[2]Department of Electrical and Computer Engineering, Ajou University, Suwon 16499, Republic of Korea

[3]These authors contributed equally

[4]Lead contact

*Correspondence:
sj0223park@ajou.ac.kr (S.P.),
jonghkim@ajou.ac.kr (J.H.K.)

https://doi.org/10.1016/j.isci.2022.104194

Figure 1. Optical, morphological properties of PTB7-Th:Y6 layers, and device structure
(A) Chemical structures of PTB7-Th and Y6, (B) UV-Vis-NIR absorption spectra of PTB7-Th, Y6, and PTB7-Th:Y6 films, (C) device structure of fabricated NIR OPD (D) energy levels of materials used in the devices (Pan et al., 2019) (Tang et al., 2019), and (E) topographic surface images of PTB7-Th:Y6 films with different additives measured by AFM (scales: one um).

its durability against external strain. Rationale of this combination is based on improvement of blocking capability of BHJ layer for injected dark charge carriers under reverse bias by providing a large energy barrier between CP and SM against dark current. As the first demonstration as NIR absorber, PTB7-Th:Y6-based NIR OPDs showed J_D of 1.16×10^{-7} A/cm^2 at -0.5 V and excellent durability of J_D against mechanical strain on the stretchable parylene substrates. Attributed to low and durable J_D, we successfully demonstrated high specific detectivity ($D^* = 2.2 \times 10^{12}$ Jones at 800 nm) NIR OPDs and highly sensitive skin-conformal photoplethysmographic (PPG) sensors.

RESULTS AND DISCUSSION

Optical properties of NIR-absorbing BHJ layers

Chemical structures of PTB7-Th and Y6 as electron-donating CP and electron-accepting SM used for this work are shown in Figure 1A. PTB7-Th:Y6 BHJ film exhibited distinct and high absorption coefficients (>1.3×10^5 cm^{-1}) at NIR wavelengths of 785–825 nm due to the strong NIR-light-absorbing properties of Y6 (Figure 1B), which is tow orders of magnitude higher than that of Si at the same range of wavelengths (Wang et al., 2018). This beneficial NIR light absorbing properties guarantee the feasibility of PTB7-Th:Y6 film as an efficient NIR sensitizer in OPD devices.

Electrical properties of NIR OPDs

Attributed to strong NIR-light-absorbing property, Y6 has been widely used as a photoactive molecule with CPs in solar cells and PDs (Zhao et al., 2020; Yuan et al., 2019). For example, Y6 was employed with PBDB-T-2F (also known as PM6) as NIR light-absorber for OPD applications. However, the devices based on PM6:Y6 exhibited very high degree of J_D (~2.0×10^{-4} A/cm^2), which impeded their PD applications despite of excellent NIR light absorption (Wei et al., 2021). In this work, to reduce J_D of Y6-based NIR OPDs, we intentionally introduced PTB7-Th as an electron donor possessing a shallower highest occupied molecular orbital (HOMO) level (5.20 eV) compared to that of PM6 (5.54 eV), which can capture injected holes under

Table 1. Device parameters for PTB7-Th:Y6 OPDs depending on different additives

Bulk Heterojunction Layer	Additives	Specific Detectivity (Jones)	Responsivity (A/W)	Dark Current Density (A/cm²)
PTB7-Th:Y6	Pristine	1.61×10^{12}	0.45	2.39×10^{-7}
	DIO	1.09×10^{12}	0.45	$5.29 10^{-7}$
	DPE	2.24×10^{12}	0.43	1.16×10^{-7}
	CN	1.11×10^{12}	0.42	4.40×10^{-7}

reverse bias condition. A schematic diagram of the device structure and energy levels of materials used in this work is shown in Figure 1C and 1D. To optimize BHJ layers, we investigated morphological changes depending on different additives (DIO, DPE, and CN) used in PTB7-Th:Y6 solutions. For this study, we performed topography mapping of the BHJ films prepared using PTB7-Th:Y6 solutions with different additives through atomic force microscopy measurements. As shown in Figure 1E, addition of DIO and DPE exhibited gradual development of nanoscale crystallization and phase separation, compared to pristine film. Addition of DPE further improved series (R_s) and shunt resistance (R_{SH}) of the devices, compared to DIO-added ones (R_S/R_{SH}) for DPE-OPD and DIO-OPD are 2.4/4.0 $\times$ 10^6ohm/cm^2 and 5.7/8.8 $\times$ 10^5 ohm/cm^2, respectively. Attributed to these beneficial effects, DPE-based OPDs exhibited the lowest dark current density and the highest specific detectivity. Meanwhile, addition of CN resulted in formation of larger size (>100–200nm) grains which hamper efficient exciton dissociation (Yuan et al., 2018), resulting in high dark current density with low responsivity and specific detectivity. Device performances depending on used additives are summarized in Table 1.

The J–V curves in Figure 2A show NIR OPD based on PTB7-Th:Y6:DPE film. For comparison, we also fabricated and measured OPDs based on PM6:Y6 BHJ layers. PTB7-Y6 devices exhibited significantly reduced J_D of 1.16×10^{-7} A/cm^2 at −0.5 V, compared to J_D (4.23×10^{-5} A/cm^2 at −0.5 V) of PM6:Y6 one, which is consistent with the previously reported results (Wei et al., 2021).

Generally, dark current of OPDs under a reverse bias condition originates from the charge carrier injection from the electrode to BHJ layer or thermally generated charge carriers in BHJ layer. Hole injection under reverse bias is known to be mostly blocked by employing ZnO hole blocking layer. However, even with hole blocking layer, high J_D values and non-ideal diode shape of J–V curves in OPDs indicate that some portion of holes can be injected to bulk heterojunction layer through defect states in solution-processed ZnO (Wei et al., 2021). In our device, by choosing PTB7-Th as a donor CP, we intentionally induced higher energy barrier (φ_B) between HOMO levels between donor and Y6 (0.42 eV), which enabled blocking of injected holes at the donor/acceptor interface and further reduced J_D, following the equation of $J_D = AT^2 \exp(−q\varphi_B/kT)$, where A, q, k, and T are the pre-exponential factor, the elementary charge, Boltzmann constant, and temperature, respectively (Yoon et al., 2017). Indeed, as shown in Figure 2A, by replacing PM6 with PTB7-Th while keeping other layers the same, dark current density was significantly reduced from 4.23×10^{-5} A/cm^2 to 1.16×10^{-7} A/cm^2. We note that PM6:Y6 layer showed higher J_D and lower φ_B (0.08 eV) compared to PTB7-Th:Y6.

Figure 2B shows external quantum efficiency (EQE) and responsivity (R) spectra of the devices. In addition to noted photocurrent density (J_{Ph}) in response to NIR (800 nm) light illumination (Figure 2A), the devices exhibited high external quantum efficiency (EQE)/responsivity (R) values of 66.8%/0.43 and 69.1%/0.45 under −0.5 and −1.0 bias, respectively, at 800 nm. The figure-of-merit of PDs is generally examined by the specific detectivity (D^*) which can be calculated following the equation of $D^* = RA^{1/2}/S_n$, where A and S_n ($i_n(\Delta f)^{-0.5}$, i_n: noise current; Δf: electrical bandwidth) are the device area and the noise spectral density, respectively. Assuming the shot noise in the J_D as the major contributor to total noise of the PDs, D^* can be obtained following the relationship $D^* = R/(2qJ_D)^{1/2}$. The D^* spectra characterized using J_D were shown in Figure 2C, and D^* values at 800 nm were obtained to be 2.2×10^{12} and 1.5×10^{12} Jones at −0.5 V and −1.0 V, respectively. For more careful noise characterization considering other noises, such as the Johnson noise and the flicker noise, we further performed direct measurements of the noise current with a noise power density (NPD) at −0.5 V and −1.0 V. NPD spectra in Figure 2D exhibited ∼1/f relation at low frequency, while they showed gradual decrease and saturated behavior or frequency-independent
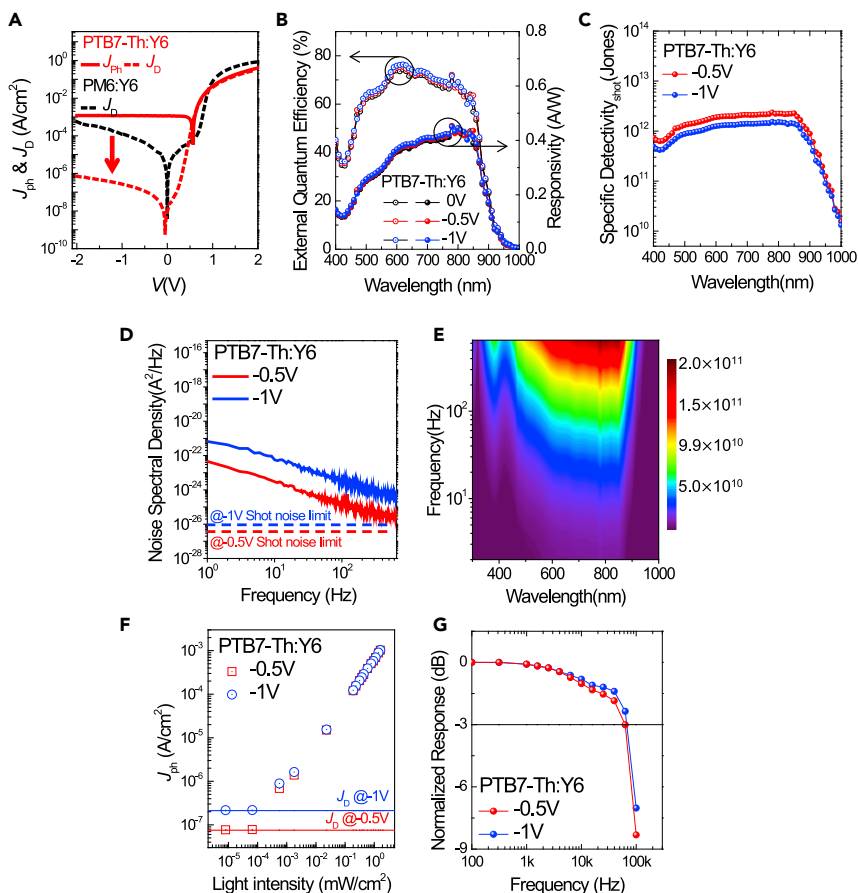
Figure 2. Electrical properties of NIR OPDs based on PTB7-Th:Y6 BHJ layers
(A) J-V curves for PTB7-Th:Y6-based NIR OPDs (black dot line: dark current density of PM6:Y6-BHJ-based OPDs),
(B) external quantum efficiency and responsivity spectra, (C) specific detectivity based on shot noise, (D) noise spectral
density, (E) 3-dimensional specific detectivity plot based on noise spectral density, (F) linear dynamic range, and (G) cut-off
frequency plot of NIR OPDs based on PTB7-Th:Y6 layers.

shapes at high-frequency region. As can be seen in Figure 2E, D^* extracted from NPD presents frequency dependence, and the highest level up to 1.9×10^{11} Jones under -0.5 V at 800 nm.

Then, to investigate reliability of the fabricated OPDs, we performed linear dynamic range (LDR) and cut-off frequency (f_{-3dB}) measurements. First, to quantify the range of operational light intensity for the devices, we assessed dependence of J_{Ph} on intensity of light. Using the obtained plot in Figure 2F and the relationship of LDR = $20\log(J_{Ph}/J_D)$, LDR levels at -0.5 and -1.0 V under 851nm NIR LED light illumination were determined to be 79 and 72 dB, respectively, which is superior to that of InGaAs-based PDs (Gong et al., 2009). We note that the device exhibited reliable LDR levels regardless of degree of applied reverse bias. Then, f_{-3dB} was determined by the frequency of input light modulation at which the device response was -3 dB lower than the low-frequency signal. The device exhibited bias-independent frequency response, i.e., consistent f_{-3dB} values around ~63.0 kHz (Figure 2G).

The device stability confirmed about humidity and thermal (Figure S3). The performance was maintained even after 1500 h under nitrogen storage. Dark current was further improved than when the device was first fabricated and measured. In the thermal stability evaluation, it was confirmed that the performance was maintained from 30° to 110°. In the case of relative humidity (RH) stability, performance changed from 20% to 71%. It was confirmed that the performance was stably maintained up to 50%, but the dark current increased after 50%. In 71% RH condition, it showed not only the increase of dark current but also the decrease of photocurrent.

Environmental and operational stability of NIR OPDs

We performed stability of our NIR-OPD devices. For the test, we monitored photocurrent and dark current density with their ratios of PTB7-Th:Y6-based OPDs under different environments. First, as can be seen in Figure R3A and B, the devices exhibited excellent stability in nitrogen environment by maintaining 98% and 27% of initial photocurrent and dark current density levels, respectively, even after ~1570 h storage. We note that reduction of dark current density during storage is likely due to the stabilization of BHJ layers with slow evaporation of residual solvent. We also examined thermal and humidity stability by examining changes of the parameters under different temperatures and relative humidities. The devices exhibited good thermal stability by maintaining 103% and 36% of initial photocurrent and dark current, respectively, at 110°C. Meanwhile, dark current density was well maintained, but gradually increased over 50% RH level due to the oxidation of the bulk heterojunction layer (Madogni et al., 2015).

Then, to investigate the dynamic stability and response speed of our OPDs, we examined static behavior (V-t) of NIR-OPDs including output voltage, extracted On/Off values with calculated frequency responsivity in response to the square-wave IR-LED (851 nm) input with a frequency of 10^{-1}–10^5 Hz (Figure S1). Rising and falling times were determined to be <0.01 ms and 0.25 ms, respectively, at frequency of 10^3 Hz. We note that the rising and falling times were extracted by calculation of lead time from 10% to 90% and from 90% to 10% of maximum value. At high frequency over 1 kHz, the output curve becomes progressively distorted and the output under the dark condition converges to the illuminated condition. Thanks to the reviewer's comment, we could verify that the devices showed a prominent photoresponse speed up to 1 kHz, indicating that the PPG signal detection with 1,000 points/sec is reliable using our NIR OPDs.

Mechanical and optical properties of ultra-thin OPDs

After performance characterization of optimized PTB7-Th:Y6-based NIR OPD devices, we investigated their applicability to skin-conformal PPG sensors. For the development of skin-attachable OPDs in application of PPG sensors, three important features should be satisfied: (i) low flexural rigidity and identical performance of ultra-flexible OPDs after delamination from supporting glass substrate, (ii) operational stability under mechanical deformation with bending radii of few micrometers scale, and (iii) robust detectivity and rapid response in the wide range of light wavelength to acquire time-resolved PPG signal from human skin. Figure 3A exhibits 3-μm-thick ultrathin OPDs on parylene after delamination from supporting glass substrate. We observed a five-order of magnitude broadening of the on/off ratio at a bias of −0.5 V with negligible performance degradation in the J-V characteristics in a dark and under illumination (AM1.5G, 100 mW/cm^2) for devices before and after delamination from supporting glass substrate as shown in Figure 3B. It indicates that the devices are well located at the neutral plane by the proper passivation layer, resulting in minimal mechanical strain during the detachment process. In addition, a low level of J_D (2.0×10^{-6} A/cm^2 at −0.5 V) was secured as well. We note that the device exhibited higher J_D compared to that on commercial ITO/glass substrates because of different resistance of sputtered ITO on stretchable parylene substrates. To confirm operational stability under mechanical deformation, we conducted an electrical and optical analysis of ultra-thin OPDs in Figure 3C. The ultra-thin OPDs were gently laminated on a 200% outward pre-stretched 500-μm-thick stretchable polymer acrylic elastomer and the uniaxial compression strain was applied inward. The compression strain is applied while decreasing the tensile strain from 200% to 0%. Consequently, the sharp multiple bending with a corrugated surface and a high aspect ratio of bending radius down to 7 μm were observed under the tensile strain of 50% (Figures 3D and 3E). With a 10% tensile strain step, parameters such as J_{sc}, J_D, and D^* maintained their initial values without significant degradation (Figures 3F and 3G) during compression (forward) and tensile (backward) deformation, which strong guarantees practical use of the device for stretchable electronics. In addition to operational stability, the transient photoresponse characteristics of ultra-thin OPDs are an important factor for high-resolution data acquisition of time-resolved PPG signals when attached to the skin surface. A wide range of −3 dB bandwidth of ~100 kHz was observed regardless of the wavelength of light, including blue (430 nm), green (565 nm), red (700 nm), and IR (851 nm) as shown in Figure 3H. Based on these results, it can be inferred that NIR-responsive ultra-thin PTB7-Th:Y6 OPDs on paryelene substrates proved the feasibility of the PPG signal detection attributed to their reliable operation under severe mechanical deformation with sensitive light responsivity in a wide range of light wavelengths.
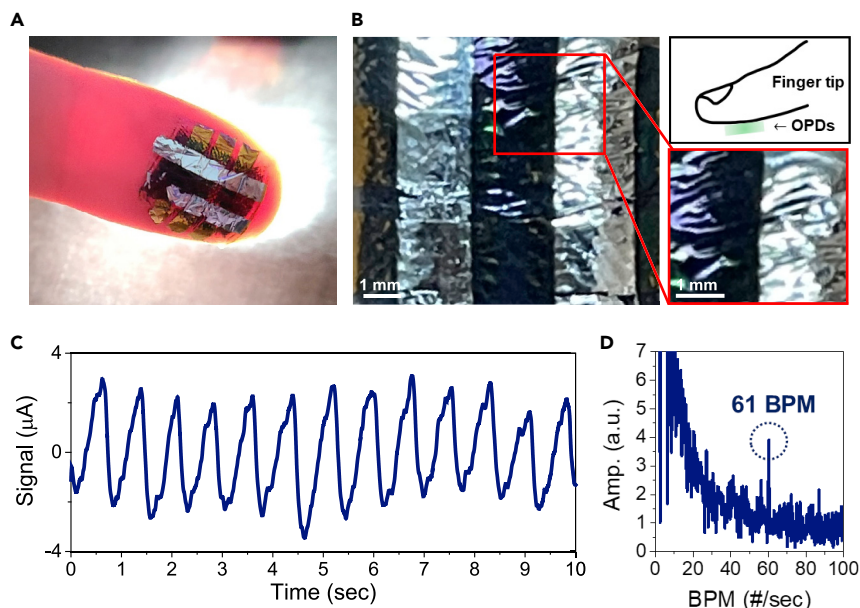
Skin-compatible NIR PPG sensors

One of the practical applications of NIR OPDs is to use their high detectivity in PPG sensors for healthcare monitoring. PPG sensors based on NIR OPDs have been developed using two device
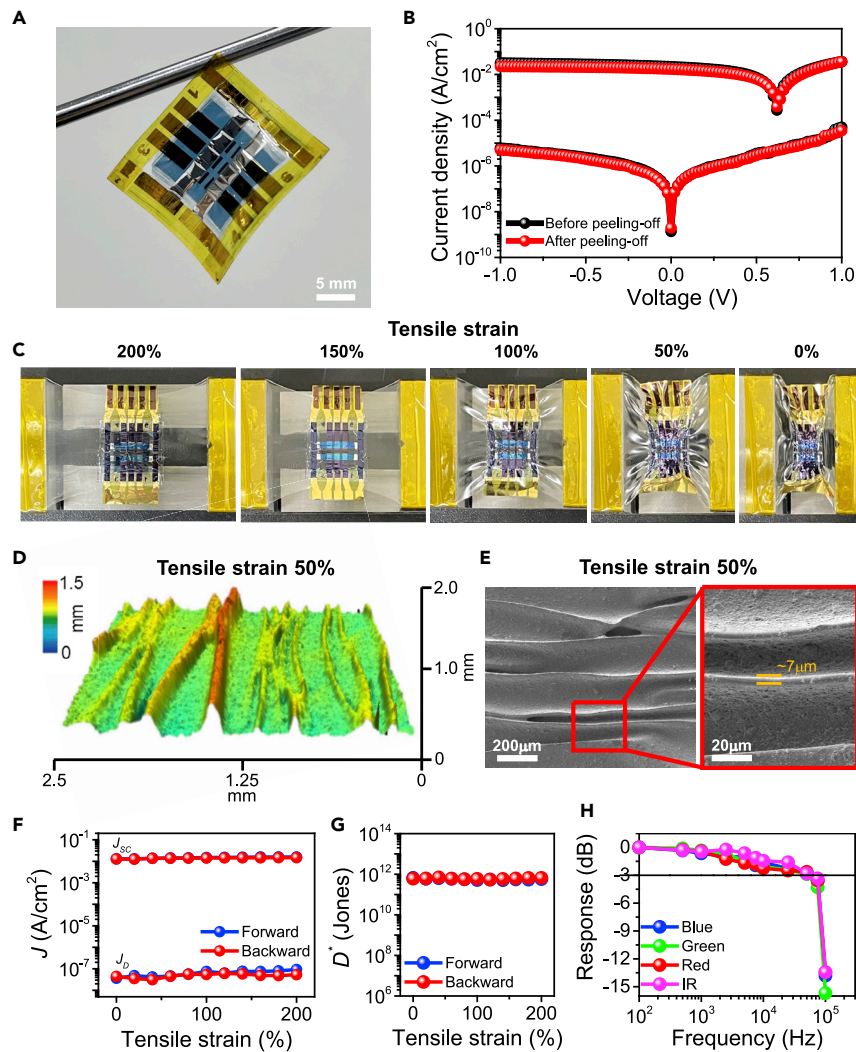
Figure 3. Mechanical and optical properties of ultra-thin OPDs

(A) Photograph of the OPD device after delamination from the supporting glass substrate.

(B) *J-V* characteristics of the OPD under solar illumination (1000 W/m^2) and dark condition before/after peeling-off.

(C) Image of an ultra-thin device laminated into a pre-stretched acrylic elastomer (200%) and compressed condition with 50% of tensile strain steps.

(D) 3D confocal microscope image of the sample at 50% of tensile strain.

(E) Top-view SEM image (left) of device surface at 50% tensile strain and enlarged image (right) indicating that the bending radius is below 7 μm. Photodiode parameters under mechanical deformation: (F) J_{SC}, J_D, under forward (compression, blue) and backward (tensile, red) (G) Specific detectivity (D^*), under mechanical deformation.

(H) Normalized response of the OPDs at blue (430 nm), green (565 nm), red (700 nm), and IR (851 nm) wavelength.

types, photodiode-type and PM-type. PPG sensors based on PM-type OPDs show excellent amplified detection signals due to high photocurrent and EQE (Zhao et al., 2021b). Meanwhile, photodiode-type-OPDs used in this work for PPG sensors exhibit relatively lower EQE levels but significantly reduced dark current, which contributes to enhance sensitivity of PPG sensors. The applicability of the OPDs comprising PTB7-Th:Y6 with high D^* and exceptional stretchability was demonstrated by fabricating skin-conformal NIR PPG, noninvasively monitoring the pulse, and determining the heart rate. Taking advantages of high D^* values of our ultra-flexible OPD devices (Figure 3G), we employed transmission mode of PPG sensing which requires high D^* because of power consumption from relatively large attenuation of light compared to reflection mode using a shorter light transport path. To assess the sensing performances, fabricated OPDs were attached to the edge of a fingertip by tightly

Figure 4. Skin-compatible NIR photoplethysmography sensors
(A) Photograph of the ultra-flexible organic photodiode attached to a bottom surface of fingertip.
(B) Conformal attachment with fingerprint (left) and position of skin-conformal photodetector under finger (right top) and enlarged image of (B) (right bottom).
(C) PPG signal detection from ultra-flexible NIR responsive organic photodiodes for 10s.
(D) Power spectrum analyzed by fast Fourier transform (FFT) signal processing. The evaluated heart rate (HR) from measured output signals exhibits 61 BPM.

covering all skin indentations due to their low flexural rigidity with a total device thickness lower than 3 μm as shown in Figures 4A and 4B. The 851 nm of IR light was illuminated to the upper skin surface of the fingertip, and ultra-flexible OPD was attached to the bottom surface of the fingertip to record the real-time volumetric change of blood vessels. Compared to conventional flexible substrates such as PET and PEN, ultra-flexible/-stretchable nature of the parylene substrates enabled both flexibility with bending radius of ~3–4 um (Figure 3E) and conformal contact with skin, which allows more sensitive PPG detection.

The continuous and periodic output signal from ultra-flexible OPD is proportional to the quantity of blood flowing through the blood vessels. In Figure 4C, we could successfully obtain clear peripheral pulse waves including explicit systolic and diastolic peaks. The heart rate (HR) can be evaluated via Fourier analysis in the frequency domain of repetitive pulsating PPG signals. From the fast Fourier transform (FFT) power spectrum, the primary peak at 61 BPM was observed which is in good agreement with those values measured for healthy adults (Jose and Collison, 1970) (Figure 4D). From these demonstrations, we concluded that the developed PTB7-Th:Y6-based OPD exhibits not only low J_D and resulting high D^* in near-IR light but also rapid response speed to NIR signals, enabling reliable and continuous PPG signal detection with low power consumption. To confirm durability of our stretchable devices against mechanical deformation for practical measurement, we tested PPG signal detection with repetitive four cycles of attachment and detachment from the skin surface (during detachment, the effective area of devices can be deformed). As displayed in Figure S2, the invariant PPG signal detection could be observed, indicating that reliable PPG signal detection can be achieved via fabricated ultra-flexible NIR OPDs.

Conclusions

In summary, we developed highly sensitive PPG sensors based on NIR OPDs which exhibited suppressed and strain-durable dark current. By combining PTB7-Th, having shallow HOMO level, with NIR-absorbing Y6 for photoactive layer, we reduced dark current through injected hole confinement effect. Finally, we

successfully demonstrated highly sensitive skin-conformal PPG sensors by constructing these OPD devices on stretchable substrates.

Limitations of the study

In this work, we designed a device architecture for suppressed and strain-durable dark current in near-infrared organic photodetectors, and demonstrated its practical applications to skin-compatible photoplethysmography sensors for the highly sensitive detection of blood volume changes in the microvascular bed of tissue. Although the devices exhibit excellent light-responsivity, detectivity, stretchability, and mechanical durability, long-term operational stability is not fully solved. Further investigations will seek to improve operational stability and resistance of sputtered ITO on stretchable substrates.

STAR★METHODS

Detailed methods are provided in the online version of this paper and include the following:

- KEY RESOURCES TABLE
- RESOURCE AVAILABILITY
  - ○ Lead contact
  - ○ Materials availability
  - ○ Data and code availability
- METHOD DETAILS
  - ○ Materials and device fabrication on glass
  - ○ Device fabrication on stretchable substrate
  - ○ Electrical characterization of OPDs
  - ○ Spectral noise analysis
  - ○ Mechanical property measurements
  - ○ Cardiovascular monitoring
- QUANTIFICATION AND STATISTICAL ANALYSIS

SUPPLEMENTAL INFORMATION

Supplemental information can be found online at https://doi.org/10.1016/j.isci.2022.104194.

AUTHOR CONTRIBUTIONS

H.J.E. and H.L. contributed equally to this work. H.J.E., H.L., Y.S., G.U.S., and A.Y.L. performed the experiments and analyzed the data. J.H., S.P., and J.H.K. conceived the project and wrote the manuscript. All authors discussed the contents and provided important contributions to the manuscript.

DECLARATION OF INTERESTS

The authors declare no competing interests.

INCLUSION AND DIVERSITY

While citing references scientifically relevant for this work, we also actively worked to promote gender balance in our reference list.

iScience
Article

REFERENCES

Chen, H., Liu, H., Zhang, Z., Hu, K., and Fang, X. (2016). Nanostructured photodetectors: from ultraviolet to terahertz. Adv. Mater. 28, 403–433. https://doi.org/10.1002/adma.201503534.

Chow, P.C.Y., and Someya, T. (2020). Organic photodetectors for next-generation wearable electronics. Adv. Mater. 32, 1902045. https://doi.org/10.1002/adma.201902045.

Gong, X., Tong, M., Xia, Y., Cai, W., Moon, J.S., Cao, Y., Yu, G., Shieh, C.-L., Nilsson, B., and Heeger, A.J. (2009). High-detectivity polymer photodetectors with spectral response from 300 nm to 1450 nm. Science 325, 1665–1667. https://doi.org/10.1126/science.1176706.

Guo, D., Yang, D., Zhao, J., Vadim, A., and Ma, D. (2020). Role of interfaces in controlling charge accumulation and injection in the photodetection performance of photomultiplication-type organic photodetectors. J. Mater. Chem. C 8, 9024–9031. https://doi.org/10.1039/D0TC01590C.

Huang, J., Lee, J., Vollbrecht, J., Brus, V.V., Dixon, A.L., Cao, D.X., Zhu, Z., Du, Z., Wang, H., Cho, K., et al. (2020). A high-performance solution-processed organic photodetector for near-infrared sensing. Adv. Mater. 32, 1906027. https://doi.org/10.1002/adma.201906027.

Jose, A.D., and Collison, D. (1970). The normal range and determinants of the intrinsic heart rate in man1. Cardiovasc. Res. 4, 160–167. https://doi.org/10.1093/cvr/4.2.160.

Kang, Y., Eun, H.J., Kye, H., Kim, D., Heo, J., Kim, J.H., and Kim, B.-G. (2020). Side-chain engineering of conjugated polymers toward highly efficient near-infrared organic photo-detectors via morphology and dark current management. J. Mater. Chem. C 8, 7765–7771. https://doi.org/10.1039/D0TC00082E.

Lee, J., Ko, S.-J., Lee, H., Huang, J., Zhu, Z., Seifrid, M., Vollbrecht, J., Brus, V.V., Karki, A., Wang, H., et al. (2019). Side-chain engineering of nonfullerene acceptors for near-infrared organic photodetectors and photovoltaics. ACS Energy Lett. 4, 1401–1409. https://doi.org/10.1021/acsenergylett.9b00721.

Li, Q., Guo, Y., and Liu, Y. (2019a). Exploration of near-infrared organic photodetectors. Chem. Mater. 31, 6359–6379. https://doi.org/10.1021/acs.chemmater.9b00966.

Li, W., Xu, Y., Meng, X., Xiao, Z., Li, R., Jiang, L., Cui, L., Zheng, M., Liu, C., Ding, L., and Lin, Q. (2019b). Visible to near-infrared photodetection based on ternary organic heterojunctions. Adv. Funct. Mater. 29, 1808948. https://doi.org/10.1002/adfm.201808948.

Li, X., Zhu, M., Du, M., Lv, Z., Zhang, L., Li, Y., Yang, Y., Yang, T., Li, X., Wang, K., et al. (2016). High detectivity graphene-silicon heterojunction photodetector. Small 12, 595–601. https://doi.org/10.1002/smll.201502336.

Liu, X., Wang, H., Yang, T., Zhang, W., Hsieh, I.-F., Cheng, S.Z.D., and Gong, X. (2012). Solution-processed near-infrared polymer photodetectors with an inverted device structure. Org. Electron. 13, 2929–2934. https://doi.org/10.1016/j.orgel.2012.08.017.

Liu, J., Gao, M., Kim, J., Zhou, Z., Chung, D.S., Yin, H., and Ye, L. (2021a). Challenges and recent advances in photodiodes-based organic photodetectors. Mater. Today 51, 475–503. https://doi.org/10.1016/j.mattod.2021.08.004.

Liu, M., Wang, J., Yang, K., Zhao, Z., Zhou, Z., Ma, Y., Shen, L., Ma, X., and Zhang, F. (2021b). Highly sensitive, broad-band organic photomultiplication-type photodetectors covering UV-Vis-NIR. J. Mater. Chem. C 9, 6357–6364. https://doi.org/10.1039/D1TC00555C.

Lu, Y., Feng, S., Wu, Z., Gao, Y., Yang, J., Zhang, Y., Hao, Z., Li, J., Li, E., Chen, H., and Lin, S. (2018). Broadband surface plasmon resonance enhanced self-powered graphene/GaAs photodetector with ultrahigh detectivity. Nano Energy 47, 140–149. https://doi.org/10.1016/j.nanoen.2018.02.056.

Lv, L., Dang, W., Wu, X., Chen, H., Wang, T., Qin, L., Wei, Z., Zhang, K., Shen, G., and Huang, H. (2020). Flexible short-wave infrared image sensors enabled by high-performance polymeric photodetectors. Macromolecules 53, 10636–10643. https://doi.org/10.1021/acs.macromol.0c01988.

Madogni, V.I., Kounouhéwa, B., Akpo, A., Agbomahéna, M., Hounkpatin, S.A., and Awanou, C.N. (2015). Comparison of degradation mechanisms in organic photovoltaic devices upon exposure to a temperate and a subequatorial climate. Chem. Phys. Lett. 640, 201–214. https://doi.org/10.1016/j.cplett.2015.09.023.

Meng, D., Zheng, R., Zhao, Y., Zhang, E., Dou, L., and Yang, Y. (2021). Near-infrared materials: the turning point of organic photovoltaics. Adv. Mater. 34, 2107330. https://doi.org/10.1002/adma.202107330.

Michel, J., Liu, J., and Kimerling, L.C. (2010). High-performance Ge-on-Si photodetectors. Nat. Photon. 4, 527–534. https://doi.org/10.1038/nphoton.2010.157.

Pan, M.-A., Lau, T.-K., Tang, Y., Wu, Y.-C., Liu, T., Li, K., Chen, M.-C., Lu, X., Ma, W., and Zhan, C. (2019). 16.7%-efficiency ternary blended organic photovoltaic cells with PCBM as the acceptor additive to increase the open-circuit voltage and phase purity. J. Mater. Chem. A 7, 20713–20722. https://doi.org/10.1039/C9TA06929A.

Park, S., Fukuda, K., Wang, M., Lee, C., Yokota, T., Jin, H., Jinno, H., Kimura, H., Zalar, P., Matsuhisa, N., et al. (2018). Ultraflexible near-infrared organic photodetectors for conformal photoplethysmogram sensors. Adv. Mater. 30,

1802359. https://doi.org/10.1002/adma.201802359.

Shkir, M., Khan, M.T., Ashraf, I.M., Almohammedi, A., Dieguez, E., and AlFaify, S. (2019). High-performance visible light photodetectors based on inorganic CZT and InCZT single crystals. Sci. Rep. 9, 12436. https://doi.org/10.1038/s41598-019-48621-3.

Simone, G., Dyson, M.J., Weijtens, C.H.L., Meskers, S.C.J., Coehoorn, R., Janssen, R.A.J., and Gelinck, G.H. (2020). On the origin of dark current in organic photodiodes. Adv. Opt. Mater. 8, 1901568. https://doi.org/10.1002/adom.201901568.

Tang, Y., Sun, H., Wu, Z., Zhang, Y., Zhang, G., Su, M., Zhou, X., Wu, X., Sun, W., Zhang, X., et al. (2019). A new wide bandgap donor polymer for efficient nonfullerene organic solar cells with a large open-circuit voltage. Adv. Sci. 6, 1901773. https://doi.org/10.1002/advs.201901773.

Wang, M., Berencén, Y., García-Hemme, E., Prucnal, S., Hübner, R., Yuan, Y., Xu, C., Rebohle, L., Böttger, R., Heller, R., et al. (2018). Extended infrared photoresponse in te-hyperdoped si at room temperature. Phys. Rev. Appl. 10, 024054. https://doi.org/10.1103/PhysRevApplied.10.024054.

Wang, Y., Gu, Y., Cui, A., Li, Q., He, T., Zhang, K., Wang, Z., Li, Z., Zhang, Z., Wu, P., et al. (2021). Fast uncooled mid-wavelength infrared photodetectors with heterostructures of van der waals on epitaxial HgCdTe. Adv. Mater. 34, 2107772. https://doi.org/10.1002/adma.202107772.

Wei, Y., Chen, H., Liu, T., Wang, S., Jiang, Y., Song, Y., Zhang, J., Zhang, X., Lu, G., Huang, F., et al. (2021). Self-powered organic photodetectors with high detectivity for near infrared light detection enabled by dark current reduction. Adv. Funct. Mater. 31, 2106326. https://doi.org/10.1002/adfm.202106326.

Wu, Z., Li, N., Eedugurala, N., Azoulay, J.D., Leem, D.-S., and Ng, T.N. (2020). Noise and detectivity limits in organic shortwave infrared photodiodes with low disorder. Npj Flex. Electron. 4, 1–8. https://doi.org/10.1038/s41528-020-0069.

Yang, W., Qiu, W., Georgitzikis, E., Simoen, E., Serron, J., Lee, J., Lieberman, I., Cheyns, D., Malinowski, P., Genoe, J., et al. (2021). Mitigating dark current for high-performance near-infrared organic photodiodes via charge blocking and defect passivation. ACS Appl. Mater. Inter. 13, 16766–16774. https://doi.org/10.1021/acsami.1c02080.

Yoon, S., Cho, J., Sim, K.M., Ha, J., and Chung, D.S. (2017). Low dark current inverted organic photodiodes using anionic polyelectrolyte as a cathode interlayer. Appl. Phys. Lett. 110, 083301. https://doi.org/10.1063/1.4977025.

Yuan, J., Xu, Y., Shi, G., Ling, X., Ying, L., Huang, F., Ho Lee, T., Young Woo, H., Young Kim, J., Cao, Y., and Ma, W. (2018). Engineering the morphology via processing additives in multiple all-polymer solar cells for improved performance. J. Mater. Chem. A. 6, 10421–10432. https://doi.org/10.1039/C8TA03343A.

Yuan, J., Zhang, Y., Zhou, L., Zhang, G., Yip, H.-L., Lau, T.-K., Lu, X., Zhu, C., Peng, H., Johnson, P.A., et al. (2019). Single-junction organic solar cell with over 15% efficiency using fused-ring acceptor with electron-deficient core. Joule 3, 1140–1151. https://doi.org/10.1016/j.joule.2019.01.004.

Zhang, S., Jiao, H., Wang, X., Chen, Y., Wang, H., Zhu, L., Jiang, W., Liu, J., Sun, L., Lin, T., et al.

(2020). Highly sensitive InSb nanosheets infrared photodetector passivated by ferroelectric polymer. Adv. Funct. Mater. 30, 2006156. https://doi.org/10.1002/adfm.202006156.

Zhao, Z., Liu, B., Xie, C., Ma, Y., Wang, J., Liu, M., Yang, K., Xu, Y., Zhang, J., Li, W., et al. (2021b). Highly sensitive, sub-microsecond polymer photodetectors for blood oxygen saturation testing. Sci. China Chem. 64, 1302–1309. https://doi.org/10.1007/s11426-021-1008-9.

Zhao, Z., Liu, M., Yang, K., Xu, C., Guan, Y., Ma, X., Wang, J., and Zhang, F. (2021a). Highly sensitive narrowband photomultiplication-type organic photodetectors prepared by transfer-printed

technology. Adv. Funct. Mater. 31, 2106009. https://doi.org/10.1002/adfm.202106009.

Zhao, Z., Wang, J., Xu, C., Yang, K., Zhao, F., Wang, K., Zhang, X., and Zhang, F. (2020). Photomultiplication type broad response organic photodetectors with one absorber layer and one multiplication layer. J. Phys. Chem. Lett. 11, 366–373. https://doi.org/10.1021/acs.jpclett.9b03323.

Zhou, X., Yang, D., and Ma, D. (2015). Extremely low dark current, high responsivity, all-polymer photodetectors with spectral response from 300 nm to 1000 nm. Adv. Opt. Mater. 3, 1570–1576. https://doi.org/10.1002/adom.201500224.

STAR★METHODS

KEY RESOURCES TABLE

REAGENT or RESOURCE	SOURCE	IDENTIFIER
Chemicals, peptides, and recombinant proteins		
Poly([2,6′-4,8-di(5-ethylhexylthienyl)benzo[1,2-b;3,3-b]dithiophene]{3-fluoro-2[(2-ethylhexyl)carbonyl]thieno[3,4-b]thiophenediyl})	One materials	CAS: 1469791-66-9
Poly[[4,8-bis[5-(2-ethylhexyl)-4-fluoro-2-thienyl]benzo[1,2-b:4,5-b′]dithiophene-2,6-diyl]-2,5-thiophenediyl[5,7-bis(2-ethylhexyl)-4,8-dioxo-4H,8H-benzo[1,2-c:4,5-c′]dithiophene-1,3-diyl]-2,5-thiophenediyl]	Derthon	CAS: 1802013-83-7
2,2′-[[12,13-Bis(2-ethylhexyl)-12,13-dihydro-3,9-diundecylbisthieno[2″,3′′:4′,5′]thieno[2′,3′:4,5]pyrrolo[3,2-e:2′,3′-g][2,1,3]benzothiadiazole-2,10-diyl]bis[methylidyne(5,6-difluoro-3-oxo-1H-indene-2,1(3H)-diylidene)]]bis[propanedinitrile]	Derthon	CAS: 2304444-49-1
Chloroform	Sigma-Aldrich	CAS: 67-66-3
Diphenyl ether	Sigma-Aldrich	CAS: 101-84-8
1-Chloronaphthalene	Sigma-Aldrich	CAS: 90-13-1
Zinc acetate dehydrate	Sigma-Aldrich	CAS: 5970-45-6
2-methoxyethanol	Sigma-Aldrich	CAS: 109-86-4
Ethanolamine	Sigma-Aldrich	CAS: 141-43-5
Molybdenum(VI) oxide	Sigma-Aldrich	CAS: 1313-27-5
Silver	iTASCO	CAS: EAG0CE0001

RESOURCE AVAILABILITY

Lead contact

Further information and requests for resources and reagents should be directed to and will be fulfilled by the lead contact, Professor Jong H. Kim (jonghkim@ajou.ac.kr).

Materials availability

This study did not generate new reagents.

Data and code availability

- All data reported in this paper will be shared by the Lead contact upon request.

- This paper does not report original code.

- Any additional information required to reanalyze the data reported in this paper is available from the Lead contact upon request.

METHOD DETAILS

Materials and device fabrication on glass

PTB7-Th (One Materials) and PM6, Y6 (Derthon) were used without further purification. Prior to the solution process, the ITO/glass substrates were cleaned by sequential sonication using detergent, de-ionized water, acetone and isopropanol for 15 min each. After sonication, UV-ozone treatment was performed for 10 min. Then, the ZnO precursor was dissolved in 2-methoxyethanol ($CH_3OCH_2CH_2OH$, Sigma-Aldrich, 1 mL) with zinc acetate dehydrate (Sigma-Aldrich, 0.1 g) and ethanolamine (Sigma-Aldrich, 0.028 mg) with stirring overnight. The prepared solution was spin-coated on the cleaned substrate, and

then heat-treated at 200°C. for 30 min. 18 mg/mL PTB7-Th:Y6 (1:1.4 wt %) mixed solution dissolved in chloroform with 1 vol % diphenyl ether added and 15 mg/mL dissolved in chloroform with 0.5 vol % 1-Chloronaphthalene added A PM6:Y6 (1:1.2 wt %) mixed solution was spin-coated (150 nm, 110nm) on ZnO on different substrates. Finally, a MoO_3 (9nm) electrode and an Ag (100nm) electrode were sequentially thermally deposited through a shadow mask in a vacuum of 2.0×10^{-6} Torr.

Device fabrication on stretchable substrate

Glass substrates were sequentially cleaned with detergent, de-ionized water, acetone, and isopropyl alcohol (IPA) for 5 min via ultrasonic treatment. After cleaning, oxygen plasma treatment was conducted for 10 min to remove residual chemicals on top of the glass surface. A fluorinated polymer layer (Novec 1700:7100, 1:10 vol %, 3M™) blend solution was spin-coated onto a cleaned glass substrate for 60 s at 2,000 rpm, and a 1-µm-thick parylene film was deposited by chemical vapor deposition (CVD) onto surface coated in the fluorinated polymer/glass substrate. After deposition of the parylene layer, the substrates were thermally annealed in a nitrogen condition for 1 h at 150°C. Subsequently, a 500-nm-thick epoxy (SU-8 3005, Micro-Chem) layer was spin-coated (5,000 rpm for 60 s) for surface planarization. The film was annealed at 95°C for 2 min 30 s after ultraviolet exposure and then annealed in a nitrogen atmosphere at 150°C for 1 h. A 100-nm-thick layer of bottom ITO electrodes was sputtered without substrate heating and patterned using a photolithography process and wet etching. A 20-nm-thick layer of zinc oxide (ZnO) layer was spin-coated for 30 s at 5,000 rpm using a precursor solution containing 1mL 2-methoxyethanol, 0.1g zinc acetate dehydrates, and 0.028 mL ethanolamine. As soon as the ZnO layer was spin-coated, the substrates were immediately displaced onto a hot-plate and annealed at 60°C to minimize aggregation of the deposited film, which was then thermally annealed in ambient air conditions for 30 min at 150°C. The active layer materials PTB7-Th:Y6 (1:1.4 wt %) were deposited in a glove box at 2,500 rpm for 60 s. MoO_3 (5 nm) and Ag (100 nm; as top electrode) were deposited sequentially by a thermal evaporator with a pressure of less than 1×10^{-5} Pa. To complete and form a passivation layer, a 1-µm-thick parylene film was deposited by CVD.

Electrical characterization of OPDs

$J-V$ curves were obtained using a semiconductor analyzer (Keithley 4200- SCS) under dark conditions and 800 nm light illumination. Spectral R values were obtained from EQE spectra of the devices, which were measured using an incident photon-to-current conversion efficiency (IPCE) setup consisting of a Xenon lamp (Newport, 450 W) and a monochromator. The current-voltage ($I-V$) characteristics were recorded under AM 1.5G (100 mW/cm^2, with the intensity calibrated using a silicon reference diode) using a Keithley 2400 source meter under ambient conditions. A typical cells device area of 0.04 cm2 was defined using a metal shadow mask. The thicknesses of the films were measured using a thickness profile meter (P-16, KLA-Tencor). The time response was recorded using a digital phosphor oscilloscope (DPO, 2024B, Tektronix) and 106 Ω of high impedance was set for measurement of the open-circuit voltage response. The LED was connected to an arbitrary function generator (AFG 3101C).

Spectral noise analysis

The noise power spectral density was obtained by the Fourier transform of dark currents at room temperature. Dark currents were measured by a semiconductor parameter analyzer (Keysight, B1500a) equipped with a wave generator/fast measurement unit (WGFMU) in a shielded dark box. The sampling frequency was set to 20 kHz so that the Nyquist frequency covers the 1/f corner frequency up to 10 kHz. For a frequency resolution of 1 Hz, 20,000 data points were recorded.

Mechanical property measurements

The freestanding ultra-flexible OPDs were laminated to a pre-stretched acrylic elastomer substrate (VHB Y-4905J, 3MTM) before measurement. To record accurate electrical signals, gold external wirings were used as the electrical contacts of the freestanding devices. The gold wirings were fabricated by deposition of 100 nm of patterned Au layers through a shadow mask onto 12.5-µm-thick polyimide films. Contact between the devices and the gold wirings was established through electrically conductive adhesive tape (ECATT 9703, 3M™). The edges of the gold wirings were connected with alligator clips. The degree of stretching was controlled using a home-made screw machine and a ruler and the measurements were conducted under ambient conditions. Data obtained from the stretching test were recorded using a Keithley 2400 source meter.

Cardiovascular monitoring

The ultra-flexible OPD was attached to a human finger. After attachment, external wiring was achieved using anisotropic conductive film (ACF) tape for electrical measurement. An LED located on the upper side of the fingertip was powered by a source meter with a biasing of 1.7 V and light intensity l000 lux, while data was recorded from an OPD located on the lower side of the fingertip using an SR570 current preamplifier and DAQami. The background output voltage was around 0 V during measurement of biological signal using PPG device, therefore we can estimate the light intensity of NIR LED through the fingertip was close to 0.1 mW/cm^2.

QUANTIFICATION AND STATISTICAL ANALYSIS

Figures represent averaged or representative results of multiple independent experiments. Analyses and plots were performed with Origin.